

# Quantifying Molecular Dynamics within Complex Cellular Morphologies using LLSM-FRAP

Huw Colin-York,\* John Heddleston, Eric Wait, Narain Karedla, Michael deSantis, Satya Khuon, Teng-Leong Chew, Ivo F. Sbalzarini, and Marco Fritzsche\*

Quantifying molecular dynamics within the context of complex cellular morphologies is essential toward understanding the inner workings and function of cells. Fluorescence recovery after photobleaching (FRAP) is one of the most broadly applied techniques to measure the reaction diffusion dynamics of molecules in living cells. FRAP measurements typically restrict themselves to single-plane image acquisition within a subcellular-sized region of interest due to the limited temporal resolution and undesirable photobleaching induced by 3D fluorescence confocal or widefield microscopy. Here, an experimental and computational pipeline combining lattice light sheet microscopy, FRAP, and numerical simulations, offering rapid and minimally invasive quantification of molecular dynamics with respect to 3D cell morphology is presented. Having the opportunity to accurately measure and interpret the dynamics of molecules in 3D with respect to cell morphology has the potential to reveal unprecedented insights into the function of living cells.

subcellular-sized region of interest (ROI), limiting its ability to investigate dynamics within the complex shapes and geometries that characterize most biological systems, e.g., the plasma membrane, cellular organelles, and the actin cytoskeleton.

In a typical FRAP experiment, a small ROI within the cell is bleached by a short exposure to high-power laser light,<sup>[5-7]</sup> and the subsequent recovery of fluorescently tagged molecules is monitored over time.<sup>[5,8]</sup> The shape of the FRAP recovery curve, the so-called mobile fraction, captures the complexity of the underlying molecular dynamics of interest. Using a theoretical model or numerical simulations of the molecular dynamics combined with knowledge of the recovery time(s) of the respective molecule, the dynamics

can be inferred.<sup>[2,9,10]</sup> Analysis of the recovery curve can reveal whether a molecule undergoes reaction kinetics or diffusion dynamics or a combination of both processes.<sup>[3]</sup> The presence of a substantial immobile fraction may result from a loss of fluorescence due to imaging, immobile molecules, or may signify that recovery has been followed over a duration that is short in comparison with the molecules' actual recovery time.<sup>[3]</sup> In FRAP, the ROI size and the image acquisition rate can be independently adjusted within a given dynamic range as offered by the microscope scanning hardware.<sup>[1,11,12]</sup> To this end, free diffusion and anomalous sub-diffusion processes can be identified and differentiated from reaction kinetics by examining recovery in regions

## 1. Introduction

Biomolecules continuously undergo reaction and diffusion dynamics in living cells. Quantification of these dynamics is profoundly important in the characterization and understanding of cellular function.<sup>[1,2]</sup> Fluorescence recovery after photobleaching (FRAP) is one of the most successful and broadly applied methodologies to quantify molecular dynamics, largely owing to its versatility to measure at sub-second time-scales, its ease of implementation, and its reliance on nonspecialist equipment.<sup>[3,4]</sup> Yet, conventional FRAP is commonly restricted to single-plane image acquisition within a

H. Colin-York, M. Fritzsche  
MRC Human Immunology Unit  
Weatherall Institute of Molecular Medicine  
University of Oxford  
Oxford OX3 9DS, UK  
E-mail: huw.colinyork@kennedy.ox.ac.uk;  
marco.fritzsche@kennedy.ox.ac.uk  
H. Colin-York, M. Fritzsche  
Kennedy Institute for Rheumatology  
University of Oxford  
Oxford OX3 7LF, UK

 The ORCID identification number(s) for the author(s) of this article can be found under <https://doi.org/10.1002/smt.d.202200149>.

© 2022 The Authors. Small Methods published by Wiley-VCH GmbH. This is an open access article under the terms of the Creative Commons Attribution License, which permits use, distribution and reproduction in any medium, provided the original work is properly cited.

DOI: 10.1002/smt.d.202200149

J. Heddleston, E. Wait, M. deSantis, S. Khuon, T.-L. Chew  
Howard Hughes Medical Institute  
Janelia Research Campus  
Ashburn VA 20147, USA  
N. Karedla, M. Fritzsche  
Rosalind Franklin Institute  
Harwell Campus  
Didcot OX11 0FA, UK  
I. F. Sbalzarini  
Faculty of Computer Science  
Technische Universität Dresden  
01187 Dresden, Germany  
I. F. Sbalzarini  
Max Planck Institute of Molecular Cell Biology and Genetics  
01307 Dresden, Germany

of different radii because reaction kinetics are length-scale independent in contrast to diffusion.<sup>[3,13]</sup> Moreover, analysis of the direction of recovery can reveal contributions of convective flow and the topology of the underlying cellular architecture.<sup>[14]</sup>

The sensitivity of FRAP is critically dependent on the acquisition rate and the loss of fluorescence due to the total illumination duration. Experimentally, the temporal resolution is imposed by the scan speed in the case of a confocal system and the camera readout speed in the case of a widefield system. Loss of fluorescence due to imaging depends on the quality of the fluorescent dye and thus the photon budget, the acquisition laser power, and the total FRAP illumination duration required to monitor full fluorescence recovery. Historically, these limitations have enforced single-plane image acquisition of subcellular regions which restricts FRAP in several ways. Single-plane imaging provides minimal information as to the wider cellular context in which the FRAP recovery takes place. Such information is important since cellular structures or organelles outside of the imaging volume may contribute to the observed recovery. Moreover, within many biological systems of interest, e.g., the plasma membrane, or cellular organelles, the distribution of molecules within the bleach ROI may not be homogenous. The distinct and highly variable geometries that define these structures vary on length scales that are often smaller than the bleach ROI, thus the quantification of their specific geometry is vital toward accurately quantifying molecular dynamics within their volume or on their surface.<sup>[15]</sup> Crucially, by imaging only a single plane, volumetric information regarding the 3D cell morphology is overlooked and as a consequence, assuming a planar geometry for the fluorescent recovery when the underlying cell geometry is curved can lead to errors in the estimation of molecular dynamics<sup>[16]</sup> (see Section S1 and Figure S1, Supporting Information). While confocal microscopy has been successfully applied to study diffusion dynamics in complex volumes and surfaces, such as the endoplasmic reticulum (ER), its acquisition speed is limited by the need to scan at each point within the sample, making the assessment of rapidly moving molecular components challenging.<sup>[15,17–19]</sup> In addition, confocal scanning introduces large amounts of light into the sample above and below the focal plane causing undesirable photobleaching and leading to difficulties interpreting fluorescence recovery.<sup>[15]</sup>

To effectively capture molecular dynamics within complex biological morphologies, a microscopy technique is required that provides good optical sectioning, minimal photobleaching, and rapid acquisition rates. Exciting fluorescence using a sheet rather than a single point of light has proved to be an effective means of circumventing many of the above limitations. This approach was utilized by Rieckher et al. in combination with FRAP to measure spatio-temporal protein dynamics in small model organisms using a light sheet of 10  $\mu\text{m}$  in thickness.<sup>[20]</sup> Similarly, a related light sheet technology, selective plane illumination microscopy, was recently combined with FRAP to measure the 2D spatial variation of intranuclear diffusion.<sup>[21]</sup> To resolve dynamics within the complex 3D cellular and subcellular environment, lattice light sheet microscopy (LLSM) uniquely maintains the optical sectioning capabilities of confocal microscopy, producing a light sheet of  $\approx 400$  nm in thickness, while gaining huge increases in acquisition speed

owing to use the camera-based acquisition.<sup>[22]</sup> These advantages were recently harnessed to examine the effects of targeted photo-stimulation within rodent hippocampal brain slices.<sup>[23]</sup> Critically, the LLSM technology permits rapid 3D imaging, providing a means to capture not only the recovery within 3D ROIs, but also to capture the wider cellular context within which the recovery takes place, facilitating the interpretation of molecular dynamics with reference to the cell as a whole.

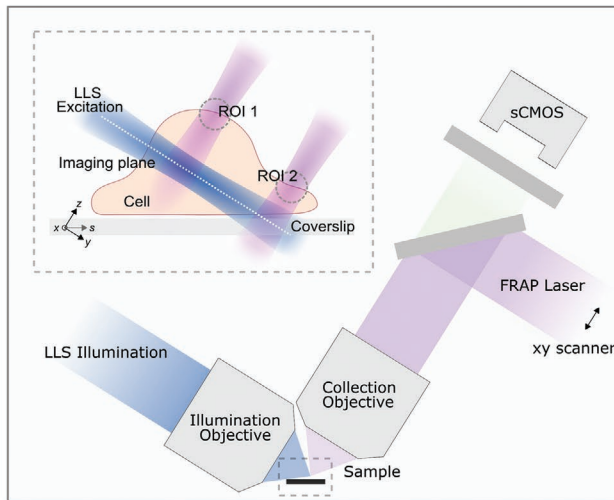
Despite recent progress in this area, there remains a need to establish a generalized experimental and analysis pipeline that permits FRAP within biological systems that exhibit complex 3D morphologies. The combination of FRAP and LLSM provides a powerful experimental platform with which to investigate molecular dynamics within such complex environments, however because it provides the potential to bleach an arbitrary volume at any desired position within the cell, it presents a significant challenge for conventional analysis pipelines. Typically, in a 2D-FRAP analysis, the intensity within the defined bleach ROI, often a circle or a square is integrated, and the resulting 1D recovery is fit using analytical expressions that are only valid for specifically defined experimental conditions.<sup>[3,4,24]</sup> In LLSM-FRAP, it is not possible to apply these established models, since the initial conditions and complex 3D morphologies resulting from the bleach are not easily formulated into an analytical expression. As a remedy, numerical simulations provide an effective means to quantify molecular dynamics within the complex morphologies that characterize biological systems.<sup>[15,17]</sup>

Here, we demonstrate the power and flexibility of combining LLSM, FRAP, and numerical simulations by investigating the diffusion dynamics of lipids and proteins in morphologically diverse regions of the cellular plasma membrane and of the cortical actin network in activating T-cells. Taking advantage of the ability of LLSM to rapidly image the whole cell volume during FRAP recovery, numerical simulations could be performed whereby the morphology of the cellular structure of interest was extracted from LLSM imaging and the transport process simulated subject to the specific 3D membrane geometry and the initial conditions defined by the FRAP bleach ROI (see the Experimental Section). We find that LLSM-FRAP can robustly extract diffusion dynamics within the low curvature apical T-cell membrane and highly curved lamellipodium during antigen stimulation. In addition, LLSM-FRAP was applied to quantify the dynamics of the actin cytoskeleton, revealing that the retrograde flow of actin at the immune synapse extended from the lamellipodial contact interface to the apical cortical actin surface of the T cell, highlighting the experimental need for robust dynamic quantification within the context of the cell, enabling novel insights into physiological molecular dynamics of living cells.

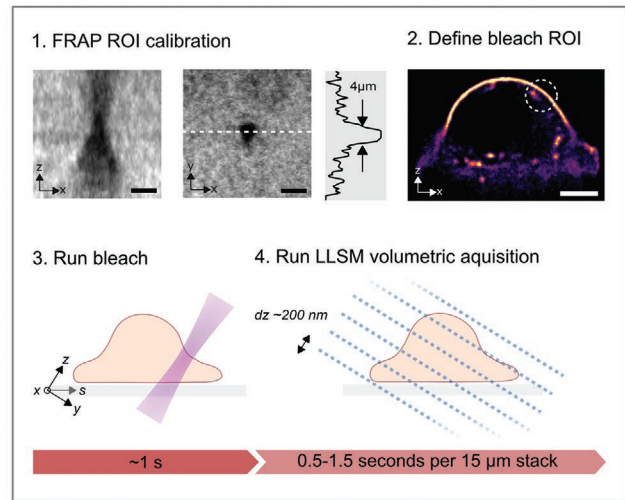
## 2. Results

To investigate molecular dynamics within the context of 3D cell morphology, we utilized the LLSM imaging platform equipped with a photobleaching laser (see Experimental Section), allowing for rapid 3D volumetric imaging of living cells in addition to control over the location and size of the photobleaching region of interest within the cell (**Figure 1a**).

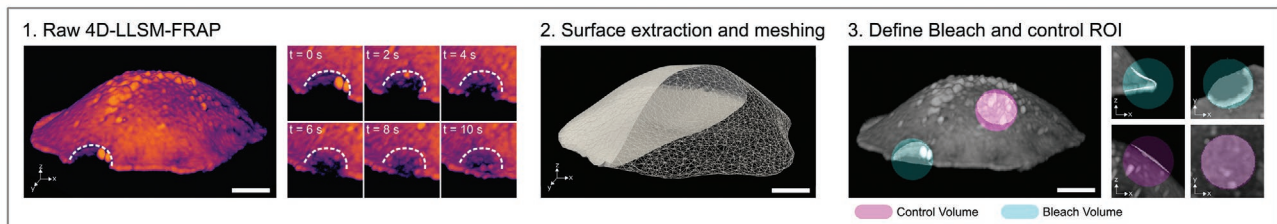
**a** LLSM-FRAP Experimental Setup



**b** Acquisition pipeline



**c** Image Analysis pipeline



**d** Simulation pipeline

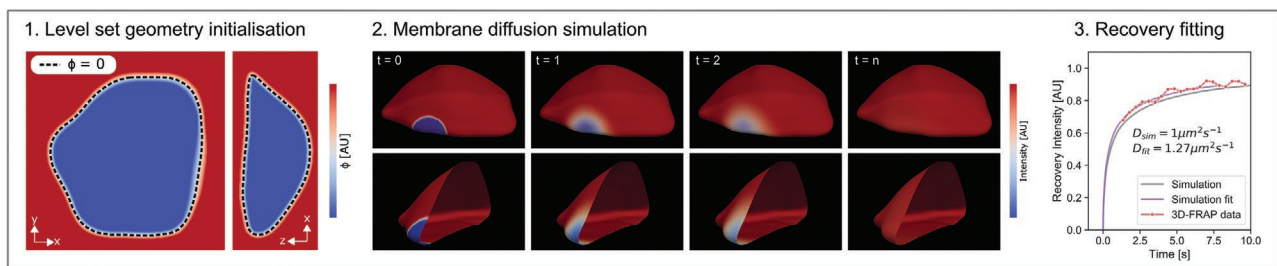


**Figure 1.** Schematic of LLSM-FRAP experiments and numerical analysis pipeline. a) Schematic outlining the LLSM-FRAP setup. A Bessel beam is laterally scanned to create a light-sheet, while piezo scanning sweeps the sample through the illuminating light sheet. Excited fluorescence light is captured by an objective whose focal plane coincides with the optical axis of the illumination light sheet. A point scanning FRAP laser is coupled into the emission objective, allowing selective bleaching at any position within the imaging volume. b) The FRAP acquisition pipeline can be outlined in four steps: 1) The bleach volume for a given laser power and duration is calibrated using dye molecules immobilized within the polyacrylamide hydrogel. Scale bar is 5  $\mu\text{m}$ . 2) After acquiring a volumetric image of the cell of interest, the bleach ROI is defined. Scale bar is 5  $\mu\text{m}$ . 3) The bleach program is executed with predefined laser power and duration. 4) LLSM imaging is initiated at sufficiently high frame rate to capture FRAP recovery. c) To extract the fluorescence recovery curve from the raw LLSM imaging (1), the cell surface is extracted, and a triangulated surface mesh defined (2). The recovered intensity is normalized to the membrane surface area within the bleach ROI (cyan) and a control ROI (magenta) is extracted to correct for photobleaching. Scale bar is 5  $\mu\text{m}$ . d) In order to quantify the diffusion coefficient of the molecule of interest, a numerical simulation is performed based on the surface geometry and bleach ROI of the cell of interest. The cell surface is defined as a level set, and a numerical method is used to solve the diffusion equation for molecules on the cell surface. The resulting simulated recovery curve is fit to the experimental data, yielding the geometry-corrected diffusion coefficient for the molecule of interest.

To illustrate the experimental power of LLSM-FRAP in combination with numerical simulations, we demonstrate its application to both lipophilic dye and membrane protein diffusion on the surface of stimulated living T-cells undergoing activation via T-cell receptor stimulation (TCR) with anti-CD3 and the formation of an immunological synapse. The dynamics of both lipids and proteins within the T-cell membrane play a key

role during T-cell activation,<sup>[25,26]</sup> yet how their dynamics varies over the cell membrane remains unclear. Specifically, when in contact with an antigen-coated surface, T-cells form a large contact area with an actin-rich lamellipodium at its periphery. Consequently, activating T-cells show distinct areas of complex surface morphology that extend in the axial direction, with the apical surface showing a low curvature, while the lamellipodial

region shows high curvature. Crucially, the diversity of morphologies exhibited by activating T-cells make the application of conventional FRAP approaches challenging, primarily due to their reliance on slow axial scanning which would fail to capture both the cell morphology and fluorescence recovery with sufficient temporal resolution. In contrast, LLSM-FRAP can capture the complex morphology of the underlying membrane and permits rapid volumetric imaging of the recovery within the context of the whole cell.

Before conducting FRAP experiments in cells, it was necessary to calibrate the photobleaching volume of the LLSM-FRAP microscope. This was done by photobleaching a polyacrylamide gel sample loaded with immobilized fluorescent dye molecules (see the Experimental Section, Figure 1b-1). By varying the photobleaching laser power, the bleach duration, and scan area, it was possible to tune the size of the photobleaching volume, which was chosen to have a diameter of  $\approx 4 \mu\text{m}$ . It should be noted that for a given bleach volume, because of the nature of the focused light, molecules above and below to focused beam are also subject to photobleaching. Crucially, in contrast to confocal-based FRAP approaches, LLSM imaging allowed for the whole cell volume to be captured at every time step, meaning the exact extent of the bleached region could be assessed for each experiment.

Following calibration, a typical LLSM-FRAP acquisition pipeline involved first selecting the cell of interest, followed by defining the shape, size, and position in 3D space of a bleach ROI (see the Experimental Section, Figure 1b-2). Next, the photobleaching program was defined based on the calibration results, specifying the duration and power of the photobleaching laser. In addition, the volumetric image acquisition parameters were defined, including the exposure time, stack number, and axial spacing. Once the microscope was set-up, the bleach program was initiated, immediately followed by the volumetric image acquisition, and continued until the bleach recovery was complete (Figure 1b-3,4). The duration of the bleach program and the time between the bleach and the volumetric image acquisition of the fluorescent recovery were minimized to avoid the undesirable effects introduced by the presence of diffusion during the bleaching phase.<sup>[9]</sup>

To quantify the dynamics of the fluorescence recovery, the recovered intensity signal was extracted from the raw LLSM imaging by analyzing the total intensity within the bleach ROI normalized to the area of the cell membrane contained within the bleach ROI (see the Experimental Section; Figure 1c). To account for the loss of fluorescence due to photobleaching of the sample, the recovery was corrected by analyzing the intensity within a control ROI, far from the bleach ROI, also normalized for the cell membrane area contained within the ROI. To achieve this, the cell surface was extracted from the raw LLSM imaging (Figure 1c-1) and transformed into a computationally defined triangular mesh (Figure 1c-2, see the Experimental Section). This allowed for the bleach and control ROIs to be defined in 3D, and their position and overlap with the surface area of the cell to be quantified (Figure 1c-3). Crucially, together with the post-bleach fluorescence distribution on the cell membrane, this computational mesh served as an input to a numerical simulation for each LLSM-FRAP experiment (Figure 1c-1). Solving the diffusion equation on the

curved plasma membrane surface allowed the evolution of the fluorescence recovery to be simulated (see the Experimental Section, Figure 1c-2). In this way, a simulated recovery curve was obtained, which could be fit to the experimental recovery curve allowing the diffusion coefficient of the species of interest to be quantified (Figure 1c-3).

To assess the mobility of the lipid component of the plasma membrane, the T-cell membrane was labeled with Cell Mask, a lipophilic dye molecule which readily incorporates into the plasma membrane of living cells. Allowing the cells to interact with a stimulating glass surface for 10 min led to the formation of stable cell contacts, mimicking the formation of the immunological synapse. To quantify the diffusion dynamics of the membrane in both the apical and lamellipodial regions, we collected a series of FRAP recordings across these two distinct zones. To avoid excessive bleaching of the total fluorescent pool within each cell, a single LLSM-FRAP acquisition was performed per cell. The initial post-bleach fluorescence distribution for a representative cell bleached in the lamellipodial region is shown in **Figure 2a**. As is clear from the XZ orthogonal view, the volumetric LLSM imaging reveals a bleach region (dashed box, Figure 2a) containing both the lower membrane in contact with the substrate and the upper side of the lamellipodium allowing the bleach area to be correctly calculated (see the Experimental Section, Figure 2a). Over the course of the 10 s recording, a full volume of the cell was acquired every 0.4 s, allowing the diffusive recovery of the Cell Mask to be tracked over time (Movie S1, Supporting Information). To extract the diffusion coefficient of the observed recovery, a simulation was defined based on the geometry of the cell surface and the initial condition of the bleach ROI. The lower panel of Figure 2a illustrates the recovery on the simulated cell surface, displaying the recovery of the bleach ROI over time (Movie S2, Supporting Information). Integrating the intensity of the recovery within the bleach region resulted in a simulated recovery curve, which was then fit in time to the experimentally acquired recovery curve (see the Experimental Section), resulting in an experimental diffusion parameter of  $1.27 \mu\text{m}^2 \text{s}^{-1}$ . Using the same approach, we next conducted a FRAP experiment where the apical surface of the activating T-cell was bleached (Figure 2b and Movie S3, Supporting Information). Similarly, the simulation and fit to experimental recovery curve resulted in an experimental diffusion coefficient of  $1.35 \mu\text{m}^2 \text{s}^{-1}$  (Figure 2b and Movie S4, Supporting Information).

By performing a series of FRAP experiments and corresponding simulations, both the diffusion and immobile fraction of Cell Mask on the surface of activating T-cells at the apical and lamellipodium surfaces were quantified (Figure 2c). The diffusion coefficient measured at the lamellipodium ( $D_{\text{LP}} = 1.09 \pm 0.33 \mu\text{m}^2 \text{s}^{-1}$ ,  $N = 3$  cells, mean and standard deviation) was slightly slower than that observed at the apical surface ( $D_{\text{A}} = 1.38 \pm 0.37 \mu\text{m}^2 \text{s}^{-1}$ ,  $N = 3$  cells, mean and standard deviation). Because LLSM allows the surface geometry of the cell to be quantified, the diffusion coefficient can be straightforwardly plotted against membrane curvature, revealing a negative correlation ( $r = -0.63$ ). Because the bleach region within the lamellipodium contained membrane regions at the basal and apical surface, we sought to investigate the diffusion coefficients within these two regions independently using a combination of

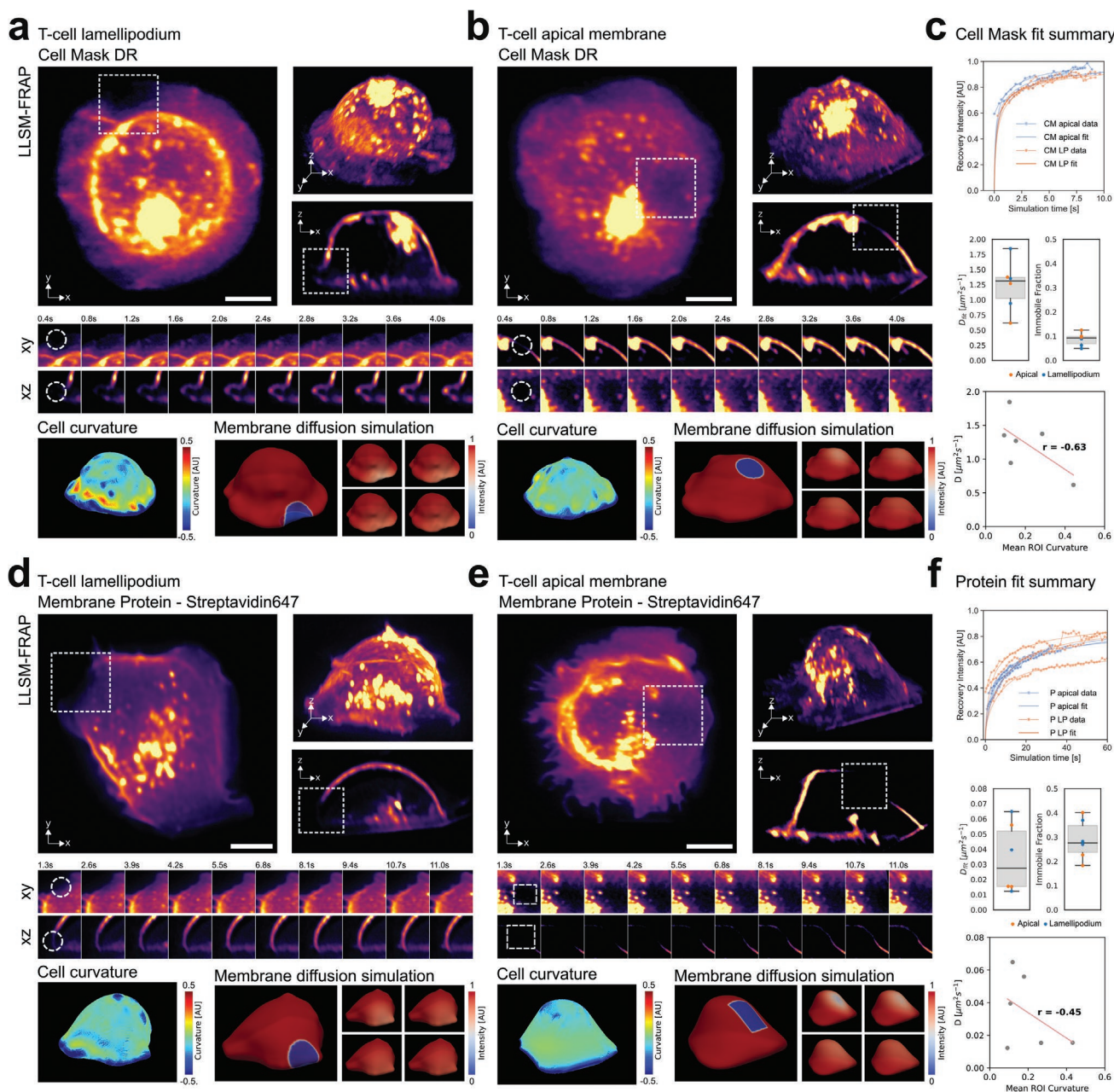


**Figure 2.** Contextual volumetric LLSM-FRAP to quantify the diffusion dynamics of biomolecules in activating T cells. a) Upper—Maximum projection, volume rendering, and vertical slice of the post bleach fluorescence distribution of Cell Mask DeepRed (DR) molecules within the membrane of an activating T-cell. The dashed box shows the bleach ROI within the lamellipodium of the cell. Scale bar is 5  $\mu\text{m}$ . Middle—temporal snapshots of the fluorescence recovery from the vertical and lateral projection of the cell membrane at the bleach ROI. White dashed region indicated the extent of the bleach ROI. Lower-left panel displays a map of the membrane mean curvature of the cell body, showing regions of high curvature at the cell lamellipodium and lower curvature of the apical surface of the cell. Lower—right panels show corresponding simulated diffusive recovery computed in the extracted cell surface geometry. The progression of the simulation over time shows the recovery of the fluorescence intensity within the bleach ROI. b) The equivalent representation of the LLSM-FRAP data as shown in part (a) but this time for a bleach ROI at the upper apical region of the cell. c) Upper—A plot showing the raw (dotted lines) and simulated (solid lines) recovery of Cell Mask within the activating T-cell membrane from both the high-curvature lamellipodial (LP) regions (orange) of the cell and the low-curvature apical surface (blue). Middle—Box plot showing the measured diffusion coefficients and immobile fraction for each region of the cell. Lower—Correlation between the diffusion coefficient and ROI membrane curvature for each cell. Panels (d)–(f) show the equivalent representations for the diffusion of biotinylated membrane proteins as labeled with Streptavidin-647 within the T-cell membrane during activation in both the lamellipodial and apical membrane.

confocal 2D-FRAP and fluorescence correlation (FCS) spectroscopy. Confocal 2D-FRAP of Cell Mask at the basal membrane of T-cells activating on anti-CD3-coated glass revealed a comparable

diffusion coefficient to those measured by LLSM-FRAP ( $D_{CF} = 1.88 \pm 0.63 \mu\text{m}^2 \text{s}^{-1}$ ,  $N = 19$  cells, median and standard deviation, Figure S2a,b, Supporting Information). Similarly,

FCS of Cell Mask diffusion under the same conditions revealed comparable values of the diffusion coefficient ( $D_{\text{FCS-Basal}} = 1.55 \pm 0.32 \mu\text{m}^2 \text{s}^{-1}$ ,  $N = 30$  cells, median and standard deviation, Figure S2c, Supporting Information). Interestingly, a similar trend to that observed using LLSM-FRAP toward faster diffusion in the apical compared to basal cell membrane was present in the FCS data, suggesting an influence of the substrate on membrane diffusion ( $D_{\text{FCS-Apical}} = 2.08 \pm 0.39 \mu\text{m}^2 \text{s}^{-1}$ ,  $N = 30$  cells, median and standard deviation). This was supported by a further decrease in the Cell Mask diffusion coefficient using a surface coating of the highly charged polymer, poly-L-lysine ( $D_{\text{FCS-Basal PLL}} = 1.18 \pm 0.27 \mu\text{m}^2 \text{s}^{-1}$ ,  $N = 29$  cells, median and standard deviation, Figure S2c, Supporting Information). Taken together, these results suggest that the overall diffusion coefficient measured by LLSM-FRAP within the lamellipodium could be influenced by both high membrane curvature at the cell periphery and membrane substrate interactions.

Next, to evaluate the corresponding diffusion of proteins within the plasma membrane, the T-cell surface was biotinylated and subsequently labeled with streptavidin conjugated to Alexa 647, fluorescently tagging proteins accessible on the cell membrane. Note, while this method presents an effective means of labeling membrane proteins, the use of streptavidin may lead to the formation of protein clusters. Again, allowing the cells to interact with a stimulating glass surface for 10 min led to the formation of stable cell contacts. Similarly, a series of FRAP experiments was conducted in the lamellipodial region (Figure 2d), as well as the apical membrane (Figure 2e and Movies S5–S8, Supporting Information). In each case, the initial bleach condition and the cell surface geometry were recovered from the raw imaging and a simulation performed, yielding a simulated recovery curve. The diffusion coefficient estimation and immobile fractions for both regions are summarized in Figure 2f. As expected, the overall rate of diffusion for the membrane proteins is around 20 x slower than for Cell Mask ( $D_A = 0.04 \pm 0.02 \mu\text{m}^2 \text{s}^{-1}$ ,  $N = 3$  cells and  $D_{\text{LP}} = 0.03 \pm 0.02 \mu\text{m}^2 \text{s}^{-1}$ ,  $N = 3$  cells, mean and standard deviation). In this case, 2D-FRAP control measurements conducted at the basal plane showed comparable values to those obtained by LLSM-FRAP ( $D_{\text{CF}} = 0.05 \pm 0.03 \mu\text{m}^2 \text{s}^{-1}$ ,  $N = 16$  cells, median and standard deviation).

Having quantified the diffusion of molecules within the plasma membrane, LLSM-FRAP was next employed to investigate directed transport phenomena in living cells. T-cell activation is known to be characterized by the centripetal retrograde flow of actin toward the center of the immunological synapse, which plays an important role in the organization and active transport of key signaling molecules.<sup>[27,28]</sup> Using LLSM-FRAP, we sought to further investigate how the filamentous actin flow varied over the surface of the whole cell during activation. By imaging the actin cytoskeleton in an activating T-cell using LLSM alone, it was possible to observe a distinct dynamic behavior; not only was the actin cytoskeleton flowing in the plane of the synapse, but a flow was also observed on the apical surface of the cell (Figure 3a,b), similar to that reported previously.<sup>[29]</sup> By tracking features on the apical surface, it was possible to crudely quantify the velocity of this flow, which was found to be  $100 \pm 40 \text{ nm s}^{-1}$ , in line with the flow rates that have been quantified at the T-cell synapse<sup>[30]</sup> (Figure 3a,b and

Movie S9, Supporting Information). Finally, taking advantage of LLSM-FRAP, an ROI was bleached near the periphery of the contact area and the recovery of the actin flow monitored over time. The bleach region recovered in a directed manner, indicating a dominant polymerization of actin at the leading edge, rather than in the bulk of the lamellipodium. Crucially, this allowed for a robust quantification of the velocity of the flow by creating a distinct feature that could be tracked with reference to the cell morphology over time (Figure 3c and Movie S10, Supporting Information). By tracking the advancing front of newly polymerizing actin at the apical surface of the cell, the flow was quantified assuming a constant velocity over the measurement zone giving a value of  $105 \pm 20 \text{ nm s}^{-1}$  ( $N = 10$  cells, mean and standard deviation), consistent with the feature tracking approach (Figure 3d,e). This result, which is in agreement with previous observations,<sup>[29]</sup> indicates that cytoskeletal flows are present at both the immunological synapse interface and on the apical surface during T-cell activation, which could have important implications for our understanding of the active transport of signaling molecules during activation.

### 3. Discussion

LLSM has provided researchers with a powerful means of assessing rapid volumetric cellular and subcellular dynamics. By combing LLSM and FRAP together with a numerical simulation analysis pipeline, we have demonstrated the ability of LLSM-FRAP to provide quantitative measurements of molecular dynamics across the volume of the cell. Crucially, by looking at the diffusion of the protein and lipid component of the plasma membrane within different regions of the T-cell membrane during activation, we have shown the potential of LLSM-FRAP to assess dynamics within morphologically complex regions of the cell.

Owing to the rapid volumetric acquisition made possible by LLSM (<1 s per cell volume), LLSM-FRAP was able to capture the local geometry of the bleach ROI as well as the wider cellular context of the dynamics of interest. This provides a key advantage over conventional widefield or confocal FRAP approaches, where limited optical sectioning or axial scanning rates restrict these modalities to very slowly evolving biological phenomena. The ability to contextualize the dynamic quantification will be critical in determining the exact structures that have been bleached, and indeed the local environment of the bleach region, including morphology, species density, and distribution, facilitating more precise and quantitative FRAP measurements. In this work, we have demonstrated the potential of combining quantification of cell morphological features, such as curvature, and dynamic measurements of membrane diffusion. While more work is required to firmly establish the correlation between these two measures, LLSM-FRAP provides a powerful platform by which to carry out such measurements. Specifically, future work should focus on investigating the molecular mechanisms that may influence diffusion dynamics within curved membranes, such as a lipid packing, protein localization, and membrane–cytoskeleton interactions.<sup>[31]</sup> It should also be noted that the finite spatial resolution inherent to fluorescence microscopy limits the spatial resolution of the

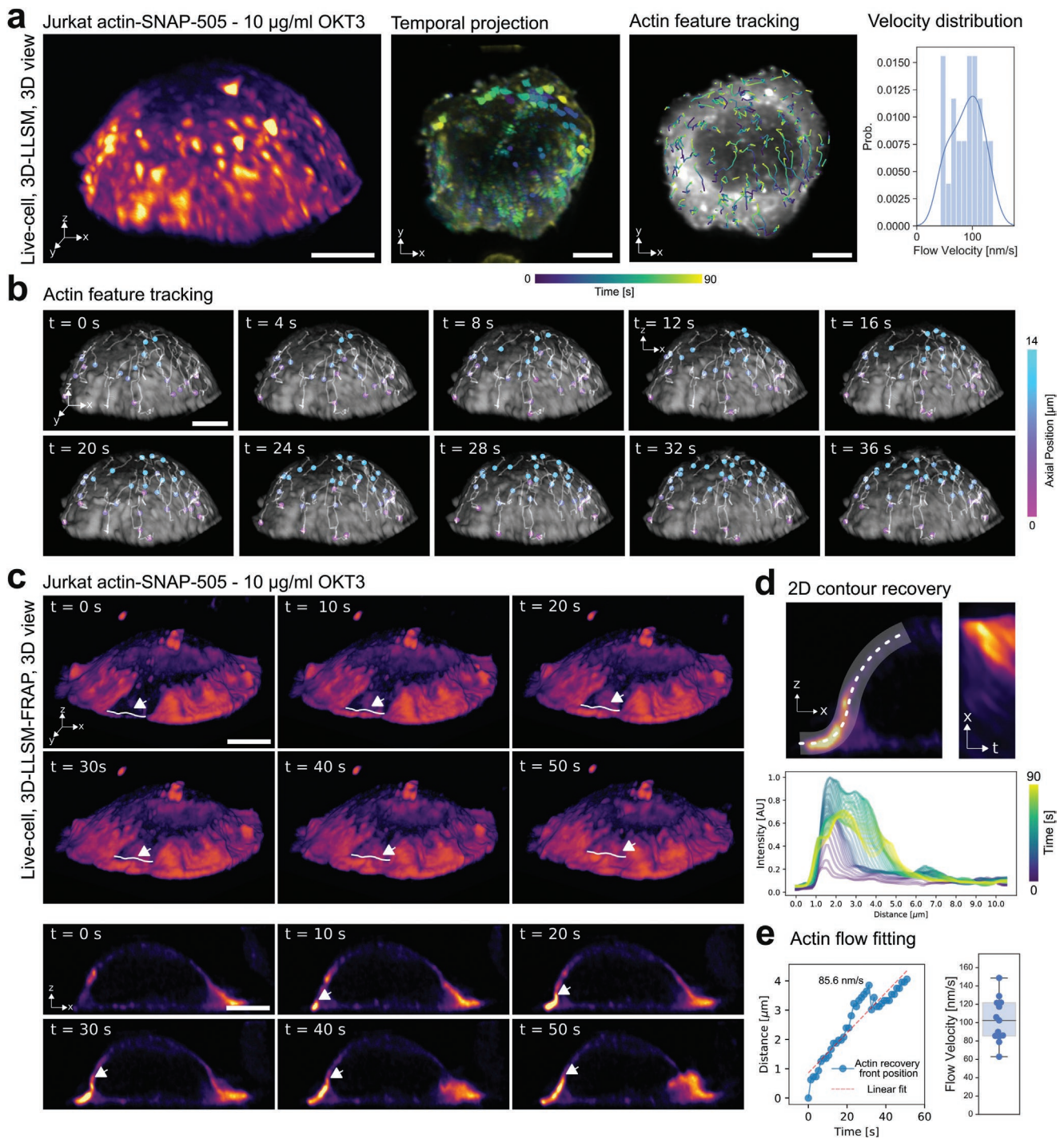


**Figure 3.** Contextual volumetric LLSM-FRAP reveals that the retrograde actin flow extends to the apical cortical surface in activating T cells. a) Left—3D projection of LLSM imaging of an activating T-cell expressing actin-SNAP and labeled with SNAP-cell-505. Middle—temporal projection of the maximum projection of the actin distribution within the T-cell. Right—Tracking of actin features on the T-cell surface over the course of the 90 s recording, together with a histogram showing the distribution of the feature velocities with a mean of  $100 \pm 40 \text{ nm s}^{-1}$ . Scale bar is  $5 \mu\text{m}$ . b) 3D projection of LLSM imaging overlaid with the 3D feature tracking, with the color of features indicating its z-position from 0 to  $14 \mu\text{m}$  at each time point. Scale bar is  $5 \mu\text{m}$ . c) Upper—3D projection snap-shots of LLSM imaging after photobleaching a volume within the lamellipodium, showing the recovery of actin at the leading edge. The white line shows the progression of the recovery at each time-step. Lower—vertical slices showing the equivalent actin recovery post bleach, indicating the flow of the actin over the apical surface of the activating T-cell. Scale bar is  $5 \mu\text{m}$ . d) Upper, left—1D contour overlay of the cell surface. Upper, right—Corresponding kymograph for the dashed contour, showing the progression of the actin recovery over the apical surface. Lower—Temporally colored line plot, showing the distribution of actin over time within the 1D contour. e) Left—A linear fit applied to the tracking of the leading edge progression of actin recovery, allowing the velocity to be quantified. Right—Quantification of the actin recovery velocity following LLSM-FRAP and 1D contour tracking, revealing a velocity of  $105 \pm 20 \text{ nm s}^{-1}$  ( $N = 10$ ).

cell morphologies extracted from the LLSM imaging, thus interpretation of diffusion on such surfaces should consider the possibility that sub-diffraction features within the membrane which may differ between the apical and basal surfaces are likely to influence the overall dynamics and concentration of membrane components.<sup>[31–33]</sup>

To extract quantitative measures of the observed dynamics, such as diffusion coefficients, because LLSM-FRAP operates in 3D+time and allows for the photobleaching of arbitrary volumes, it necessitates a numerical simulation approach. In the current work, only freely diffusing molecules were considered to contribute to the fluorescent recovery, thus any recovery that was a consequence of other transport phenomena could lead to errors within the analysis pipeline. To increase the generality of this approach, future works should be directed at allowing for the simulation of other transport processes, e.g., reaction and convection processes.<sup>[34]</sup> In addition, in this study, diffusion was restricted to the surface of the cell, thus coupled reaction–diffusion processes between membrane and the cytoplasm were not considered. Extending the simulation framework to considerations of reaction kinetics would provide an elegant way forward allowing to investigate reaction–diffusion processes in the cytosol as well as any coupling between cytoskeletal dynamics and membrane bound proteins and lipids.

Complementary to the quantification of diffusion dynamics, LLSM-FRAP allows for directed transport phenomena to be determined from the LLSM imaging. We investigated the retrograde flow of the lamellipodial and cortical actin cytoskeleton associated with immunological synapse formation. LLSM-FRAP provided a robust means of quantifying the actin flow rate at the T-cell surface, which would be very challenging to achieve using other widefield or confocal FRAP approaches, primarily due to their limited acquisition rates in 3D and the associated increases in photobleaching and photo-toxicity. Intriguingly, LLSM imaging revealed that the actin flow was present at the basal contact area of cell, consistent with previous observations, but also extended to the apical cortical actin surface.<sup>[29,30]</sup> The retrograde flow of actin at the immune synapse has been shown to be crucial for controlling the active transport of key signaling molecules, such as the T-cell receptor. Thus, the presence of this flow observed over the apical surface of the cell may be important in restricting transport or facilitating the transport of other molecules away from the contact interface at the immunological synapse.

To further extend the application of LLSM-FRAP, the microscopy would benefit from improvements in aberration correction and sample-adaptive optics, allowing well-defined FRAP bleach regions to be defined deep within more complex biological samples, moving beyond single cells to tissue and organisms *in vivo*.<sup>[34]</sup> Quantifying reaction and diffusion dynamics of biomolecules with specificity to the context of their cellular and/or tissue environment may thus become the method of choice to further our understanding of the inner workings and function of living cells and their surroundings.

LLSM-FRAP provides an experimental and computational framework for quantifying contextualized molecular dynamics applicable to many cell and tissue types. The combination of dynamic techniques like FRAP with LLSM represents a powerful path toward understanding molecular dynamics within

the native cellular environment and paves the way for the combination of other dynamic techniques with advanced volumetric imaging offering the potential to open-up unprecedented insights into molecular physiology of living cells.<sup>[35]</sup>

## 4. Experimental Section

**Cell Culture:** Jurkat T cells were cultured in sterile RPMI (Sigma-Aldrich) supplemented with 10% FCS (Sigma-Aldrich),  $2 \times 10^{-3}$  M L-glutamine (Sigma-Aldrich),  $1 \times 10^{-3}$  M sodium pyruvate (Sigma-Aldrich),  $10 \times 10^{-3}$  M Hepes (Sigma-Aldrich), and 1% penicillin-streptomycin-neomycin solution (Sigma-Aldrich). Cells were maintained at 37 °C and 5% CO<sub>2</sub> during culturing, and handling was performed in HEPA-filtered microbiological safety cabinets. Typically, cells were kept at a density between  $5 \times 10^5$  and  $9 \times 10^5$  cells mL<sup>-1</sup>.

**Cell Transduction:** Jurkat-T cell lines stably expressing SNAP-actin were generated using a lentiviral transduction strategy. HEK-293T cells were plated in six-well plates at  $3 \times 10^5$  cells mL<sup>-1</sup>, 2 L per well in Dulbecco's modified Eagle's medium (Sigma-Aldrich) + 10% FCS. Cells were incubated for 24 h at 37 °C and 5% CO<sub>2</sub> before transfection with lentiviral packaging vectors p8.91 and pMD.G and the relevant pHR-SIN lentiviral expression vector using Genejuice (Merck Millipore) as per the manufacturer's instructions. 48 h after transfection, the cell supernatant was harvested and filtered using a 0.45 mm Millex-GP syringe filter unit to remove detached HEK-293T cells. 3 mL of this virus-containing medium was added to  $1.5 \times 10^6$  Jurkat T cells in 3 mL of supplemented RPMI medium. After 48 h, cells were moved into 10 mL of supplemented RPMI and passaged as normal.

**Cell Fluorescence Labeling:** Dynamics of the plasma membrane were monitored by Cell Mask Deep Red (ThermoFisher, UK). Fluorescence labeling was achieved by first washing  $1 \times 10^6$  Jurkat T-cells three times in phosphate-buffered saline (PBS), followed by resuspension in 1 mL Leibnowitz (L-15) medium (Merck, UK) containing a 1:10 000 dilution of Cell Mask Deep Red ( $0.5 \mu\text{g mL}^{-1}$ ). Cells were then incubated with the dye solution for 10 min at 37 °C. Cells were then centrifuged and resuspended in fresh L15 and imaged immediately.

Cell surface biotinylation was achieved by first washing  $1 \times 10^6$  Jurkat T-cells three times in PBS, followed by resuspension in 1 mL PBS containing  $2 \times 10^{-3}$  M of the cell-impermeable biotinylation reagent EZ-Link Sulfo-NHS-LC-Biotin (ThermoFisher, UK), targeting primary amines present on cell membrane proteins. Cells were incubated in the biotinylation solution for 30 min at room temperature (RT). Cells were then washed three times with PBS to remove any unbound Sulfo-NHS-LC-Biotin. To visualize the membrane proteins using LLSM, the biotinylated cells were incubated with a solution of Streptavidin-Alexa-647 (ThermoFisher, UK) at a concentration of  $10 \mu\text{g mL}^{-1}$  for 30 min at RT. Cells were then centrifuged and washed to remove excess Streptavidin-Alexa-647, resuspended in fresh L15 and imaged immediately.

Monomeric actin labeling was achieved by incubating SNAP-actin expressing Jurkat T-cells with a  $5 \times 10^{-6}$  M solution of SNAP-cell-505 (NEB, USA), for 30 min at 37 °C. Excess dye was removed by washing three times in L15 prior to imaging.

**Coverslip Preparation:** Microscope coverslips were functionalized for T-cell activation experiments by coating with anti-CD3 (OKT3, eBioscience, UK). Coverslips with a diameter of 5 or 18 mm diameter (#1 thickness, Warner Instruments and #1.5 thickness, SLS, USA) were coated with a  $10 \mu\text{g mL}^{-1}$  solution of OKT3 or a  $10 \mu\text{g mL}^{-1}$  poly-L-lysine overnight at 4 °C. Coverslips were washed with  $3 \times 1$  mL of PBS before use.

**LLSM Image Acquisition:** LLSM imaging was performed at the Advanced Imaging Center, Howard Hughes Medical Institute, Janelia Research Campus, VA, using a custom-built system described in the study of Chen et al.<sup>[22]</sup> Anti-CD3-functionalized 5 mm coverslips were secured in a custom-made surgical steel holder onto a piezo stage (Physik Instrumente, Germany) and fluorescently tagged Jurkat T cells were dispensed above the coverslip into the medium bath prior to each

experiment. All experiments were performed at 37 °C and 5% CO<sub>2</sub>. Once a cell of interest was within the focal plane of the light sheet, the imaging was initiated with the sample laterally scanned through the light sheet. All microscope hardware was controlled by Labview control software. The total scan distance was ranged from 0 to 15 μm at 10 to 40 ms exposure. Light was collected from the single excitation plane by a 1.1 numerical aperture (NA) 25 × water-dipping objective (Nikon) and recorded on an Orca Flash4.0 V2 sCMOS camera (Hamamatsu). The minimum and maximum NA of the LLSM pattern was 0.44 and 0.55, respectively. Cells were excited by either 488 (SNAP-505) or 647 nm (Cell Mask DeepRed and Streptavidin-Alexa-647) wavelength laser light at 1% to 5% acousto-optic tuneable filter transmittance of 300 and 500 mW laser power (MPB Communications, USA). Following data acquisition, all images were deskewed to correct for the 31.8° angle of the detection objective relative to the vertical axis of the sample and run through multiple iterations of a Richardson-Lucy deconvolution algorithm. Volumetric rendering and 4D visualization were carried out using napari, a multi-dimensional image viewer for Python.<sup>[36]</sup>

**LLSM-FRAP:** The LLSM-FRAP optical setup allowed the simultaneous execution of FRAP and LLSM experiments in living cells. FRAP was carried out using an FRAP UGA-42-Firefly laser unit (Rapp OptoElectronic, Germany) coupled to the emission 1.1 NA 25 × water-dipping objective of the LLSM system. This optical system generated a diffraction-limited bleach spot which could be scanned laterally to generate a bleach region of the desired shape and size, enabling rapid sequential photobleaching of an ROI and subsequent volumetric imaging within the imaging volume of the LLSM. The FRAP protocol can be described as follows: first, a cell of interest was located using LLSM imaging generating a pre-bleach image of the cell. Next, using the Rapp SysCon software, pre-calibrated to the dimensions of the LLSM imaging output, a bleach ROI of a defined shape and size was drawn on the pre-bleached image of the cell. The bleach program was then selected, including laser power (40% of max), duration (100–1000 ms), and repeats (1x). The bleach program parameters were selected based on the results of the bleach calibration (see below). Once the bleach program was defined, it was initiated and LLSM imaging was resumed immediately following its completion. The frame rate of the LLSM acquisition was optimized for the molecular species of interest and the signal to noise of the resulting image volume, ranging from 0.4 to 3 s per volume.

To assess the size of the bleach spot, a calibration was performed using FITC-labeled polyacrylamide gel prepared as described in ref. [37]. The immobilized dye molecules allowed the 3D bleach volume to be assessed for a given laser power and exposure time.

**LLSM-FRAP Analysis:** To extract the diffusion coefficients from the raw LLSM acquisition, it was necessary to computationally extract both the fluorescence recovery within the plasma membrane coinciding with the bleach volume, and to extract the geometry of the plasma membrane across the whole cell. Using these inputs allowed numerical simulations to be performed and the diffusion parameters estimated. The details of each step within the analysis pipeline are explained in detail in the following.

First, to extract a surface representing the plasma membrane of the cell, the pre-bleach LLSM volumetric intensity image was binarized, resulting in a binary volume equal to 1 inside of the cell and 0 outside. Next, to transform the binary volume into a triangulated mesh, a marching cubes algorithm was applied (*skimage.measure.marching\_cubes*, scikit-image v.0.19.0), resulting in a closed triangulated iso-surface mesh at the cell boundary which could be exported in the standard .ply format. Post processing of the mesh, including smoothing (100 iterations of Taubin smoothing with  $\mu = 0.1$  and  $\lambda = 0.5$ <sup>[38]</sup>) and the calculation of the surface mean curvature<sup>[39]</sup> was performed in the Meshlab software package.<sup>[40]</sup> Having established the location of the plasma membrane within the volumetric image, a spherical bleach volume was defined, centered on the intensity minimum within the bleached region of the LLSM image. The dimensions of the bleach region were matched to those acquired using the polyacrylamide calibration sample. The intersection between the bleach volume and the plasma membrane surface allowed the area of the membrane within

the bleach volume to be established. Thus, by dividing the integrated intensity within the bleach volume by the intersecting membrane area, the average intensity per unit area of the ROI membrane as a function of time could be extracted, representing the experimentally acquired recovery curve. A volume outside of the bleach ROI was also selected to normalize for the pre-bleach intensity per unit area of the membrane and for any photobleaching.

To determine the diffusion coefficients from the experimentally acquired recovery curves, it was necessary to carry out numerical simulations that capture the curved surface geometry of the cell and the bleach ROI. To simulate the diffusive recovery of both Cell Mask and the membrane proteins in the curved membrane surface, a numerical simulation algorithm implemented in FORTRAN-90 based on the Parallel Particle Mesh (PPM) Library was used.<sup>[15,17,41]</sup> The same computer code had previously been used to simulate diffusive FRAP recovery on curved membranes and is comprehensively detailed in ref. [17]. For completeness, a brief description of the methods is provided here. The simulation can be subdivided into three steps. First, the .ply mesh extracted from the LLSM imaging was transformed into a level set function defined in the volumetric domain matching the LLSM image volume, with the zero level set defining the surface of the cell and an underlying mesh resolution of  $k = 0.1 \mu\text{m}$ . Next, particles, possessing both a position and a mass, were created within a narrow band around the zero-level set (band radius =  $5k$ ), whose initial mass was defined to match the observed distribution of fluorescence molecules in the post-bleach LLSM image. The diffusion of fluorescent molecules was then simulated by the transfer of mass between the particles, as governed by the underlying isotropic continuum diffusion equation discretized using the Particle Strength Exchange method,<sup>[17]</sup> with diffusion coefficient,  $D_{\text{sim}}$  set to  $1 \mu\text{m}^2 \text{s}^{-1}$  constrained to the direction tangential to the membrane. At each time step, the mass within the bleach ROI was numerically integrated, leading to a fluorescence recovery curve. The convergence of the numerical simulation was verified for a known analytical solution in Figure S3 in the Supporting Information, as demonstrated in ref. [17]. Volumetric rendering and 4D visualization of the simulations were performed using ParaView.<sup>[42]</sup>

Lastly, the resulting simulated FRAP recovery curve was fit to the normalized experimental data by stretching in time, optimizing the objective function  $\min_{\Sigma} |F_{\text{sim}}(f \cdot t_{\text{sim}}) - F_{\text{data}}(t_{\text{data}} + d)|$  using the Python function *scipy.optimize.minimize* from the SciPy library v.1.5.2, where  $F_{\text{sim}}$  denotes the simulated mean fluorescence within the bleach ROI,  $F_{\text{data}}$  the mean fluorescence within the bleach ROI extracted from the LLSM imaging,  $t_{\text{sim}}$  and  $t_{\text{data}}$  represent the simulation and experiment time-scale, and  $d$  is the delay between the bleach and recovery acquisition. The value of  $f$  was then used to scale the diffusion coefficient between the experimental and simulated data ( $D_{\text{fit}} = D_{\text{sim}}/f$ ).

**Conventional 2D-FRAP:** Conventional 2D-FRAP experiments were conducted using a Leica SP8 confocal microscope equipped with an HC PL APO 100 × 1.40 NA oil objective and environmental control maintaining a temperature of 37 °C in and an atmosphere of 5% CO<sub>2</sub>. For each FRAP acquisition, a 2 μm diameter circular bleach region was defined and following an initial bleach period at 100% laser intensity, the fluorescence recovery was monitored for a further 40 s at a frame rate of 2.2 s<sup>-1</sup>. Further details for the optimization of FRAP experiments are presented in Fritzsche and Charras.<sup>[3]</sup> Fitting of the normalized diffusive FRAP recovery was performed in Python using *scipy.optimize.curve\_fit* implementing the Soumpasis fit<sup>[24]</sup> for a uniform 2D circular bleach ROI:

$$F(t) = F_0 + F_{\text{mob}} e^{-\frac{2\tau_D}{t}} \left( I_0 \left( \frac{2\tau_D}{t} \right) + I_1 \left( \frac{2\tau_D}{t} \right) \right)$$
, where  $F_0$  denotes the post-bleach intensity,  $F_{\text{mob}}$  the mobile fraction,  $\tau_D$  the characteristic diffusion time,  $I_0$  and  $I_1$  are modified Bessel functions of the first kind.

**Fluorescence Correlation Spectroscopy:** Confocal FCS measurements were acquired on a Zeiss 980 confocal microscope equipped with a Zeiss 40x C-Apochromat NA 1.2 W Corr objective. Prior to the FCS measurement, Jurkat T cells were loaded with Cell Mask Deep Red, at a concentration of 0.5 μg mL<sup>-1</sup>. FCS recordings were directly controlled by the Zeiss Zen Blue software and fluorescent light from recordings in both the apical and basal membrane was collected onto a GaAsP

detector (Channel S) in photon counting mode, with the pinhole set to 1 airy unit. To translate transit times to diffusion coefficients, the width of the microscope PSF was quantified using a  $10 \times 10^{-9}$  M solution of ATTO655-COOH, with a known diffusion coefficient of  $426 \pm 8 \mu\text{m}^2 \text{s}^{-1}$ .<sup>[43]</sup> FCS data were fit with a 2D diffusion model using the FoCuS-point fitting software.<sup>[44]</sup>

**Actin Velocity Quantification:** Actin velocity quantification of raw LLSM images was performed using custom written code written in Python and based on the tracking library known as Trackpy (<http://soft-matter.github.io/trackpy/v0.4.2/>). The algorithm permits the localization of spherical features of a user defined size and intensity range in each volume of the time-lapse (*tp.batch*). Defining a minimum displacement between frames, and a minimum track length, the code linked individual localizations into tracks allowing the actin velocity to be estimated (*tp.link\_df* and *tp.filter\_stubs*).

Actin velocity quantification of LLSM-FRAP data was performed using a kymograph approach. For each bleached cell, an xz slice was extracted from the 3D volume, allowing the recovery of the actin intensity within the lamellipodium and over the apical surface of the cell to be visualized. Next, a contour was plotted aligned to the cell surface and a kymograph calculated, producing an evolution of the actin intensity over the contour through the recovery. Tracking and plotting the leading edge of the recovering actin intensity over time and applying a linear fit permitted the quantitation of the actin velocity.

**Statistics:** LLSM-FRAP experiments of Cell Mask and membrane protein diffusion in activating T-cells and their corresponding numerical simulations were carried out in 3 cells per condition, with a total of 12 cells. LLSM-FRAP experiments quantifying actin retrograde flow within the lamellipodium and cortical actin of activating T-cell were carried out in a total of 10 cells.

## Supporting Information

Supporting Information is available from the Wiley Online Library or from the author.

## Acknowledgements

M.F., H.C.Y., and N.K. acknowledge generous funding from the Rosalind Franklin Institute and the Kennedy Trust for Rheumatology Research, the Wolfson Imaging Centre Oxford for providing microscope facility support, as well as the Wellcome Trust (212343/Z/18/Z), and the EPSRC (EP/S004459/1). The Advanced Imaging Center at Janelia Research Campus is supported by the Gordon and Betty Moore Foundation as well as the Howard Hughes Medical Institute.

## Conflict of Interest

The authors declare no conflict of interest.

## Data Availability Statement

The data that support the findings of this study are available from the corresponding author upon reasonable request.

## Keywords

actin cytoskeleton, diffusion, FRAP, lattice light sheet microscopy, membranes

Received: February 1, 2022  
Published online:

- [1] S. Kondo, T. Miura, *Science* **2010**, 329, 1616.
- [2] M. Fritzsche, A. Lewalle, T. Duke, K. Kruse, G. Charras, *Mol. Biol. Cell* **2013**, 24, 757.
- [3] M. Fritzsche, G. Charras, *Nat. Protoc.* **2015**, 10, 660.
- [4] D. Axelrod, D. E. Koppel, J. Schlessinger, E. Elson, W. W. Webb, *Biophys. J.* **1976**, 16, 1055.
- [5] D. Blumenthal, L. Goldstien, M. Edidin, L. A. Gheber, *Sci. Rep.* **2015**, 5, 11655.
- [6] K. C. Mudumbi, E. C. Schirmer, W. Yang, *Nat. Commun.* **2016**, 7, 12562.
- [7] B. L. Sprague, R. L. Pego, D. A. Stavreva, J. G. McNally, *Biophys. J.* **2004**, 86, 3473.
- [8] E. A. J. Reits, J. J. Neefjes, *Nat. Cell Biol.* **2001**, 3, E145.
- [9] M. Kang, C. A. Day, A. K. Kenworthy, E. Dibeneditto, *Traffic* **2012**, 13, 1589.
- [10] A. Bläßle, G. Soh, T. Braun, D. Mörsdorf, H. Preiß, B. M. Jordan, P. Müller, *Nat. Commun.* **2018**, 9, 1582.
- [11] H. Lemcke, J. Peukert, N. Voronina, A. Skorska, G. Steinhoff, R. David, *J. Mol. Cell. Cardiol.* **2016**, 98, 117.
- [12] S. Dorsch, K.-N. Klotz, S. Engelhardt, M. J. Lohse, M. Bünemann, *Nat. Methods* **2009**, 6, 225.
- [13] S. Condamine, V. Tejedor, R. Voituriez, O. Bénichou, J. Klafter, *Proc. Natl. Acad. Sci. USA* **2008**, 105, 5675.
- [14] M. Fritzsche, D. Li, H. Colin-York, V. T. Chang, E. Moeendarbary, J. H. Felce, E. Sezgin, G. Charras, E. Betzig, C. Eggeling, *Nat. Commun.* **2017**, 8, 14347.
- [15] I. F. Sbalzarini, A. Mezzacasa, A. Helenius, P. Koumoutsakos, *Biophys. J.* **2005**, 89, 1482.
- [16] B. M. Aizenbud, N. D. Gershon, *Biophys. J.* **1982**, 38, 287.
- [17] I. F. Sbalzarini, A. Hayer, A. Helenius, P. Koumoutsakos, *Biophys. J.* **2006**, 90, 878.
- [18] J. L. Kingsley, J. P. Bibeau, S. I. Mousavi, C. Unsal, Z. Chen, X. Huang, L. Vidali, E. Tüzel, *Biophys. J.* **2018**, 114, 1153.
- [19] C. J. S. Klaus, K. Raghunathan, E. Dibeneditto, A. K. Kenworthy, *Mol. Biol. Cell* **2016**, 27, 3937.
- [20] M. Rieckher, I. Kyparissidis-Kokkinidis, A. Zacharopoulos, G. Kourmoulakis, N. Tavernarakis, J. Ripoll, G. Zacharakis, *PLoS One* **2015**, 10, e0127869.
- [21] C. M. Hobson, E. T. O'Brien, M. R. Falvo, R. Superfine, *Biophys. J.* **2020**, 119, 514.
- [22] B.-C. Chen, W. R. Legant, K. Wang, L. Shao, D. E. Milkie, M. W. Davidson, C. Janetopoulos, X. S. Wu, J. A. Hammer, Z. Liu, B. P. English, Y. Mimori-Kiyosue, D. P. Romero, A. T. Ritter, J. Lippincott-Schwartz, L. Fritz-Laylin, R. D. Mullins, D. M. Mitchell, J. N. Bembek, A.-C. Reymann, R. Böhme, S. W. Grill, J. T. Wang, G. Seydoux, U. S. Tulu, D. P. Kiehart, E. Betzig, *Science* **2014**, 346, 1257998.
- [23] M. Ducros, A. Getz, M. Arizono, V. Pecoraro, M. Fernandez-Monreal, M. Letellier, U. Valentin Nägerl, D. Choquet, *Proc. SPIE* **2019**, 10865, 1086508.
- [24] D. M. Soumpasis, *Biophys. J.* **1983**, 41, 95.
- [25] M. M. Davis, M. Krogsgaard, J. B. Huppa, C. Sumen, M. A. Purbhoo, D. J. Irvine, L. C. Wu, L. Ehrlich, *Annu. Rev. Biochem.* **2003**, 72, 717.
- [26] M. L. Dustin, *Cancer Immunol. Res.* **2014**, 2, 1023.
- [27] Y. Yu, A. A. Smoligovets, J. T. Groves, *J. Cell Sci.* **2013**, 126, 1049.
- [28] H. Colin-York, S. Kumari, L. Barbieri, L. Cords, M. Fritzsche, *J. Cell Sci.* **2019**, 133, jcs232322.
- [29] A. T. Ritter, Y. Asano, J. C. Stinchcombe, N. M. G. Dieckmann, B.-C. Chen, C. Gawden-Bone, S. Van Engelenburg, W. Legant, L. Gao, M. W. Davidson, E. Betzig, J. Lippincott-Schwartz, G. M. Griffiths, *Immunity* **2015**, 42, 864.
- [30] H. Colin-York, Y. Javanmardi, M. Skamrahl, S. Kumari, V. T. Chang, S. Khuon, A. Taylor, T.-L. Chew, E. Betzig, E. Moeendarbary, V. Cerundolo, C. Eggeling, M. Fritzsche, *Cell Rep.* **2019**, 26, 3369.
- [31] A. Callan-Jones, P. Bassereau, *Curr. Opin. Solid State Mater. Sci.* **2013**, 17, 143.

- [32] S. Sadeghi, M. Müller, R. L. C. Vink, *Biophys. J.* **2014**, *107*, 1591.
- [33] R. Rojas Molina, S. Liese, A. Carlson, *Biophys. J.* **2021**, *120*, 424.
- [34] P. Incardona, A. Leo, Y. Zaluzhnyi, R. Ramaswamy, I. F. Sbalzarini, *Comput. Phys. Commun.* **2019**, *241*, 155.
- [35] J. Rosenberg, G. Cao, F. Borja-Prieto, J. Huang, *Cell Syst.* **2020**, *10*, 433.
- [36] N. Sofroniew, T. Lambert, K. Evans, J. Nunez-Iglesias, K. Yamauchi, A. C. Solak, G. Buckley, G. Bokota, T. Tung, Ziyangczi, J. Freeman, P. Boone, P. Winston, L. Royer, H. Har-Gil, S. Axelrod, A. Rokem, Bryant, Hector, M. Huang, P. Vemuri, R. Dunham, Jakirkham, A. de Siqueira, B. Chopra, C. Wood, C. Gohlke, D. Bennett, DragaDoncila, E. Perlman, *napari/napari: 0.3.5*, CERN European Organization for Nuclear Research, Switzerland **2020**.
- [37] H. Colin-York, C. Eggeling, M. Fritzsche, *Nat. Protoc.* **2017**, *12*, 783.
- [38] G. Taubin, in *Proc. ACM SIGGRAPH Conf. Computer Graphics* (Eds: S. G. Mair, R. Cook), Association for Computing Machinery, New York, NY, USA **1995**, pp. 351–358.
- [39] M. Meyer, M. Desbrun, P. Schröder, A. H. Barr, in *Visualization and Mathematics III* (Eds: H. C. Hege, K. Polthier), Springer, Berlin, Heidelberg **2003**, pp. 35–37.
- [40] P. Cignoni, M. Callieri, M. Corsini, M. Dellepiane, F. Ganovelli, G. Ranzuglia, in *Eurographics Italian Chapter Conf.* (Eds: V. Scarano, R. D. Chiara, U. Erra), The Eurographics Association, Switzerland **2008**, pp. 129–136.
- [41] I. F. Sbalzarini, J. H. Walther, M. Bergdorf, S. E. Hieber, E. M. Kotsalis, P. Koumoutsakos, *J. Comput. Phys.* **2006**, *215*, 566.
- [42] J. Ahrens, B. Geveci, C. Law, *ParaView: An End-User Tool for Large Data Visualization*, Vol. 836, Los Alamos National Laboratory **2005**.
- [43] C. B. Müller, A. Loman, V. Pacheco, F. Koberling, D. Willbold, W. Richtering, J. Enderlein, *EPL* **2008**, *83*, 46001.
- [44] D. Waithe, M. P. Clausen, E. Sezgin, C. Eggeling, *Bioinformatics* **2016**, *32*, 958.